Supporting Information for "The Land-Ocean Contrast in Deep Convective Intensity in a Global Storm-Resolving Model"

Tristan H. Abbott^{1,2}, Nadir Jeevanjee³, Kai-Yuan Chen¹, Linjiong Zhou¹,

Lucas Harris³

¹Cooperative Institute for Modeling Earth Systems, Princeton University, Princeton, NJ, USA

²Now at Breakthrough Energy, 4110 Carillon Point, Kirkland, WA USA

³NOAA/Geophysical Fluid Dynamics Laboratory, Princeton, NJ, USA

Contents of this file

- 1. Text S1 to S3
- 2. Data Set S1
- 3. Figures S1 to S12

Text S1: Land-ocean Contrast in X-SHiELD Reflectivity

Unlike lightning (which is not simulated by GSRMs) and updraft velocities (which are not observed globally), reflectivity-based proxies for intense convection can be computed from GSRM and observed by satellite. For this reason, we initially assumed that reflectivity would be a key part of our evaluation of the land-ocean contrast in GSRM simulations. As shown in this section, however, X-SHiELD produces a fairly muted land-ocean contrast in reflectivity-based proxies for intense deep convection, even in simulations with a very

clear land-ocean contrast in the frequency of strong updrafts. We argue that this is caused by a surprisingly weak relationship between simulated updraft velocity and reflectivity, and that this may be a consequence of constraints on the fall speeds of large hydrometeors imposed by the use of a bulk microphysics scheme.

We compute simulated reflectivity fields from X-SHiELD output by computing reflectivity factors based on the particle size distributions used by X-SHiELD's microphysics scheme, and convert reflectivity factors to equivalent reflectivity following Stoelinga (2005). We include rain, snow, and graupel in the reflectivity calculation, and assume that snow and graupel particles are coated by a layer of liquid water at temperatures above freezing.

We compare the distribution of observed 40 dBZ echoes above 6.5 km—a proxy for intense deep convection analyzed in Section 2 in the main text—with the distribution of strong simulated echoes above 6.5 km. To account for uncertainties associated with the droplet size distribution imposed by X-SHiELD's single-moment microphysics scheme, which may bias simulated reflectivity in strong updrafts relative to observations, we compare results using 40 dBZ and 50 dBZ as the threshold that defines a "strong" simulated echo.

In the X-SHiELD simulation with parameterized shallow convection enabled, neither the frequency of 40 dBZ nor 50 dBZ echoes above 6.5 km show a clear land-ocean contrast (Figures S1 and S2). The absolute frequency of simulated 40 dBZ echoes above 6.5 km agrees reasonably well (within a factor of 3) with observations over tropical land, given the constraints imposed by the use of a single-moment microphysics scheme. The disagreement is much larger over tropical oceans, where X-SHiELD produces 40 dBZ echoes above 6.5

km well over an order of magnitude more frequently than is observed. The lack of a landocean contrast in this X-SHiELD simulation persists when using 50 dBZ as the threshold for a strong simulated echo.

In the X-SHiELD simulation with parameterized shallow convection disabled, the landocean contrast in reflectivity-based proxies for intense convection remains fairly weak
(Figures S1 and S3) despite a much stronger land-ocean contrast in the frequency of strong
updrafts. To illustrate why a much stronger land-ocean contrast in updraft velocities does
not produce a land-ocean contrast in reflectivity-based proxies for intense convection, we
compute joint histograms of layer-maximum vertical velocity and reflectivity within a
kilometer-thick layer between 6 and 7 km (Figure S4a). These joint histograms show
that, in X-SHiELD, high reflectivity frequently occurs outside of strong updrafts between
6 and 7 km, and therefore is a fairly poor predictor of the presence of a strong updraft.

The relatively weak relationship between reflectivity and updraft velocity in X-SHiELD may be at least partially related to the use of a single-moment microphysics scheme that is unable to simulate hydrometeor size sorting. In nature, larger hydrometeors fall more quickly than smaller ones. In the X-SHiELD microphysics scheme, in contrast, sedimentation transports all hydrometeors (of a given species in a given grid cell) downward with a single bulk fall speed, calculated as a mass-weighted integral of the terminal fall speeds of hydrometeors with different sizes (Zhou et al., 2022). This limits the fall speed of the largest hydrometeors, which contribute the most to simulated reflectivity, and may make it easier for relatively weak updrafts to suspend large hydrometeors and maintain high reflectivity. To test the plausibility of this idea, we run an additional X-SHiELD simulation with parameterized shallow convection disabled and with hydrometeor terminal fall

speeds fixed to 20 m s⁻¹. This is a significant increase relative to the maximum terminal velocities allowed in the default X-SHiELD microphysics scheme (12 m s⁻¹; Zhou et al., 2022, Table 1), and we emphasize that this is not intended to be a realistic terminal fall speed for large hydrometeors. Rather, it is intended to produce a simulation where hydrometeors can only be suspended by very strong updrafts. Due to computational constraints, we run this simulation for just 10 days beginning on 1 August 2016, and discard only the first two days of output for spin-up.

Setting hydrometeor terminal fall speeds to 20 m s⁻¹ produces a much stronger relationship between vertical velocity and reflectivity. Compared with the simulation using default fall speeds, the simulation with 20 m s⁻¹ fall speeds produces much fewer strong (40-50 dBZ) echoes outside of strong updrafts (Figure S4b). Setting fall speeds to 20 m s⁻¹ has little effect on the distribution of intense updrafts; like the simulation with default fall speeds, it produces clear land-ocean differences in the frequency of 20 m s⁻¹ updrafts and 12 m s⁻¹ updrafts below 500 hPa (see Figure 2 in the main text). The land-ocean contrast in updraft velocities, plus the stronger relationship between updraft velocity and reflectivity produced by high fall speeds, allows the simulation with 20 m s⁻¹ fall speeds to produce a somewhat clearer land-ocean contrast in the frequency of 40 dBZ echoes above 6.5 km, and a strong land-ocean contrast (index above 10) in the frequency of 50 dBZ echoes above 6.5 km (Figure S1 and S5).

The simulation with 20 m s⁻¹ fall speeds does not perfectly capture the land-ocean contrast in observed reflectivity statistics, and we again emphasize that we are not suggesting that fixed 20 m s⁻¹ fall speeds are a realistic choice for GSRMs. We also note that the lack of size sorting in X-SHiELD's single-moment microphysics scheme may not be a complete

explanation for the seemingly unrealistic insensitivity of reflectivity to updraft velocity. A number of past studies document a tendency for kilometer-scale models to overestimate radar reflectivity both in simulations with single-moment microphysics schemes (Blossey et al., 2007; Lang et al., 2007; Li et al., 2008; Matsui et al., 2009; Caine et al., 2013) and two moment bulk and bin microphysics schemes (Varble et al., 2011, 2014; Stanford et al., 2017). Even if fall speeds of large hydrometeors were predicted accurately, past work has shown that biases in updraft width that limit condensate fallout (Varble et al., 2014), errors in parameterizations of microphysical processes (Stanford et al., 2017; Qu et al., 2022), and assumptions about particle size distributions and mass-diameter relationships (Varble et al., 2011, 2014) can also lead to high biases in simulated reflectivity, and the importance of these factors versus insufficient size sorting in X-SHiELD's single-moment microphysics scheme is unclear.

Text S2: Frequency of Events Associated with Observed versus Simulated Land-Ocean Contrasts

As a second check on the realism of the land-ocean contrast simulated by X-SHiELD with parameterized shallow convection disabled, we compare the observed frequency of electrified convection over tropical land with the frequency of strong simulated updrafts. Rather than calculating raw counts of lightning flashes and updrafts (which are difficult to compare directly, since individual updrafts do not necessarily produce a single lightning flash), we instead compare the frequency of thunder days in ground station records with the frequency of simulated "updraft days", defined as days when the X-SHiELD simulation produces a strong updraft close to the location of a ground station.

We use ground station records from the NOAA Global Surface Summary of the Day between 11 August and 8 September 2016, the same period for which we analyze X-SHiELD output. This provides daily summaries of meteorological observations for over 9000 stations across the globe, including a flag that indicates whether a station recorded audible thunder on a given day. We aggregate ground station records in 10°-by-10° latitude-longitude bins and compute a single thunder-day frequency for each bin by dividing the number of station-days with recorded audible thunder by the total number of station-days. We omit bins that contain fewer than 5 stations.

We compare observed thunder-day frequencies with the frequency of strong simulated updrafts by saving daily-maximum column-maximum updraft speeds during the X-SHiELD simulation with parameterized shallow convection disabled. (Note that this is an online diagnostic based on continuous monitoring of simulated updraft speeds, not an offline calculation based on 3 hourly snapshots.) We compute a record of "updraft days" by checking, on each day and at the location of each GSOD station, whether the daily-maximum column-maximum updraft speed is above a given threshold in any column less than 15 km from the station location. 15 km is an estimate of the typical distance over which thunder is audible (Brooks, 1925; Fleagle, 1949; Lavigne et al., 2019). We then aggregate records in 10°-by-10° latitude-longitude bins to compute simulated updraft-day frequencies to compare to observed thunder-day frequencies.

Observed thunder-day frequencies are between about 10% and 60% in convectively active regions over tropical land (Figure S6a). Simulated " 20 m s^{-1} updraft day frequencies", derived from X-SHiELD output by searching for updraft speeds above 20 m s^{-1} are lower than observed thunder day frequencies by about a factor of 4 (Figure S6b), suggesting that

20 m s⁻¹ updrafts in X-SHiELD are somewhat less frequent than lightning in observations. The same is likely true for 12 m s⁻¹ updrafts below 500 hPa, which occur in 3D snapshots with frequencies comparable to 20 m s⁻¹ updrafts. 10 m s⁻¹ updraft day frequencies, derived from X-SHiELD by searching for updraft speeds above 10 m s⁻¹, are comparable to observed thunder day frequencies with the exception of Western Africa, where observed thunder-day frequencies are higher (Figure S6c). However, X-SHiELD does not produce a land-ocean contrast in the frequency of 10 m s⁻¹ updrafts (recall Figure 2a). This suggests that, even with parameterized shallow convection disabled, X-SHiELD may be "missing" a land-ocean contrast in the frequency of moderately-strong convective events that are about as common as electrified convection in nature.

Text S3: Identification and Analysis of Widths of 3D Updrafts

Our analysis of low-level updraft widths (Section 2) failed to reveal substantial differences between land and ocean. Here, so show that a more complicated analysis of 3D updraft objects (again, in the X-SHiELD simulation with parameterized shallow convection disabled) provides a similar result.

Our 3D updraft identification algorith proceeds as follows. We initially identify updrafts as contiguous three-dimensional regions on the X-SHiELD native grid with cloud condensate mass fraction $q_c > 10^{-5}$ kg kg⁻¹ and vertical velocity w > 1 m s⁻¹. We then refine the boundary of each updraft by setting the vertical velocity threshold for that updraft to $w_{max}/2$, where w_{max} is the updraft-maximum vertical velocity. If this splits the original updraft into multiple contiguous regions, we keep only the region that contains the grid cell where we found w_{max} for the original updraft.

The motivation for this refinement step is to avoid introducing spurious correlations between updraft width and intensity. To understand this, consider a horizontal slice through a hypothetical axisymmetric updraft with vertical velocity given by $w(r) = w_{max} f(r/L)$, where r is the horizontal distance from the center of the updraft, w_{max} is the vertical velocity at the center of the updraft, and f is a horizontal structure function that decays with radius over a length scale L. L is clearly the parameter that controls the width of this hypothetical updraft, and we would like the width of the region identified as within the updraft to depend only on L. However, if we identify updrafts by masking a region with w above a fixed threshold w_t , the radius of the masked region will depend on both L and w_{max} , and will increase with w_{max} even if L is fixed. If we instead make w_t proportional to w_{max} , the radius of the masked region will depend only on L. We use a relatively restrictive threshold of $w_t = w_{max}/2$ because we found that lower thresholds often failed to separate nearby updrafts in organized convective systems. Finally, we emphasize that the low-level updraft identification algorithm described in the main text uses a fixed 1 m s⁻¹ vertical velocity threshold with no refinement. The similarity between results from algorithms with and without an adaptive threshold provides evidence that the use of an adaptive threshold is not producing fundamentally misleading results.

We identify tropical updrafts by processing each equatorial face of the cubed-sphere individually. To handle updrafts that overlap the edges of the cubed sphere, we add 64 grid points of padding from adjacent faces to the east and west edges of each face, treat the outermost 64 grid points on the north and south edges of each face as padding, and only retain updrafts with w_{max} outside of the padding. We save w_{max} for each updraft, and in addition save the maximum updraft width (defined as $\sqrt{A_{max}}$, where A_{max} is the

maximum horizontal cross-sectional area of the updraft), the mean updraft width (defined as $\sqrt{V/H}$, where V is the updraft volume and H is the updraft height), and the minimum distance between the updraft core and clear air (defined as the minimum distance between the grid cell with updraft-maximum vertical velocity and any grid cell on the same model level with less than 10^{-5} kg kg⁻¹ of cloud condensate). Finally, as in the low-level updraft identification algorithm, we discard all updrafts that are outside of the tropical land and ocean regions defined in Section 2.1 in the main text. Figure S10 shows the locations of the remaining updrafts after further filtering for $w_{max} > 2$ m s⁻¹, $w_{max} > 12$ m s⁻¹, and $w_{max} > 20$ m s⁻¹.

Histograms of 3D updraft widths inside the tropical land and ocean regions show no evidence for a systematic difference between land and ocean (Figure S11 first and second columns). Like low-level updrafts, almost all 3D updrafts are between 1 and 3 grid cells wide, and the shapes of 3D updraft width distributions are nearly identical over land and ocean. Histograms of the minimum distance between updraft cores and clear air (a measure of cloud width) provide no evidence that wider clouds over land prevent updraft dilution by shielding updraft cores from surrounding clear air (Figure S11 third column). Cloud width distributions peak at distances corresponding to 1-3 grid cells, indicating that most updraft cores (which are themselves grid-scale) are in clouds that are only a few grid cells wide. These results are strikingly insensitive to the minimum w_{max} (2 m s⁻¹, 12 m s⁻¹, and 20 m s⁻¹ in Figure S11a-c, d-f, and g-i, respectively). Subsetting for updrafts with w_{max} above 12 or 20 m s⁻¹ does reveal a noticeably longer tail of wide clouds (Figure S11, third columns), possibly because very strong updrafts tend to occur in the upper

X - 10 :

troposphere where detrainment produces horizontally-extensive anvil clouds. However, distributions of cloud widths are similar over land and ocean at all w_{max} thresholds.

Data Set S1. Full-resolution versions of images from Figures 6 and 11 from the main text. Each pixel in full-resolution images corresponds to a single model grid cell.

References

- Blossey, P. N., Bretherton, C. S., Cetrone, J., & Kharoutdinov, M. (2007). Cloud-resolving model simulations of kwajex: Model sensitivities and comparisons with satellite and radar observations. *Journal of the Atmospheric Sciences*, 64(5), 1488–1508.
- Brooks, C. E. P. (1925). The distribution of thunderstorms over the globe. *Geophysical Memoirs London*, 24, 147-164.
- Caine, S., Lane, T. P., May, P. T., Jakob, C., Siems, S. T., Manton, M. J., & Pinto, J. (2013). Statistical assessment of tropical convection-permitting model simulations using a cell-tracking algorithm. *Monthly Weather Review*, 141(2), 557–581.
- Fleagle, R. G. (1949). The audibility of thunder. The Journal of the Acoustical Society of America, 21(4), 411–412.
- Lang, S., Tao, W., Simpson, J., Cifelli, R., Rutledge, S., Olson, W., & Halverson, J. (2007). Improving simulations of convective systems from trmm lba: Easterly and westerly regimes. *Journal of the atmospheric sciences*, 64(4), 1141–1164.
- Lavigne, T., Liu, C., & Liu, N. (2019). How does the trend in thunder days relate to the variation of lightning flash density? *Journal of Geophysical Research: Atmospheres*, 124(9), 4955–4974.
- Li, Y., Zipser, E. J., Krueger, S. K., & Zulauf, M. A. (2008). Cloud-resolving modeling

of deep convection during kwajex. part i: Comparison to trmm satellite and ground-based radar observations. *Monthly weather review*, 136(7), 2699–2712.

- Matsui, T., Zeng, X., Tao, W.-K., Masunaga, H., Olson, W. S., & Lang, S. (2009). Evaluation of long-term cloud-resolving model simulations using satellite radiance observations and multifrequency satellite simulators. *Journal of Atmospheric and Oceanic Technology*, 26(7), 1261–1274.
- Qu, Z., Korolev, A., Milbrandt, J. A., Heckman, I., Huang, Y., McFarquhar, G. M., ... Nguyen, C. (2022). The impacts of secondary ice production on microphysics and dynamics in tropical convection. *Atmospheric Chemistry and Physics*, 22(18), 12287–12310.
- Stanford, M. W., Varble, A., Zipser, E., Strapp, J. W., Leroy, D., Schwarzenboeck, A., ... Protat, A. (2017). A ubiquitous ice size bias in simulations of tropical deep convection. *Atmospheric Chemistry and Physics*, 17(15), 9599–9621.
- Stoelinga, M. T. (2005). Simulated equivalent reflectivity factor as currently formulated in rip: Description and possible improvements. White paper, 5. Retrieved from https://citeseerx.ist.psu.edu/document?repid=rep1\&type=pdf\&doi=decaba07f1fbb53a5fe52f5093662213af8063c4
- Varble, A., Fridlind, A. M., Zipser, E. J., Ackerman, A. S., Chaboureau, J.-P., Fan, J., ... Shipway, B. (2011). Evaluation of cloud-resolving model intercomparison simulations using twp-ice observations: Precipitation and cloud structure. *Journal of Geophysical Research: Atmospheres*, 116(D12).
- Varble, A., Zipser, E. J., Fridlind, A. M., Zhu, P., Ackerman, A. S., Chaboureau, J.-P., ... Shipway, B. (2014). Evaluation of cloud-resolving and limited area model in-

tercomparison simulations using TWP-ICE observations: 1. deep convective updraft properties. *Journal of Geophysical Research: Atmospheres*, 119(24), 13–891.

Zhou, L., Harris, L., Chen, J.-H., Gao, K., Guo, H., Xiang, B., ... Morin, M. (2022). Improving global weather prediction in GFDL SHiELD through an upgraded GFDL cloud microphysics scheme. *Journal of Advances in Modeling Earth Systems*, 14(7), e2021MS002971.

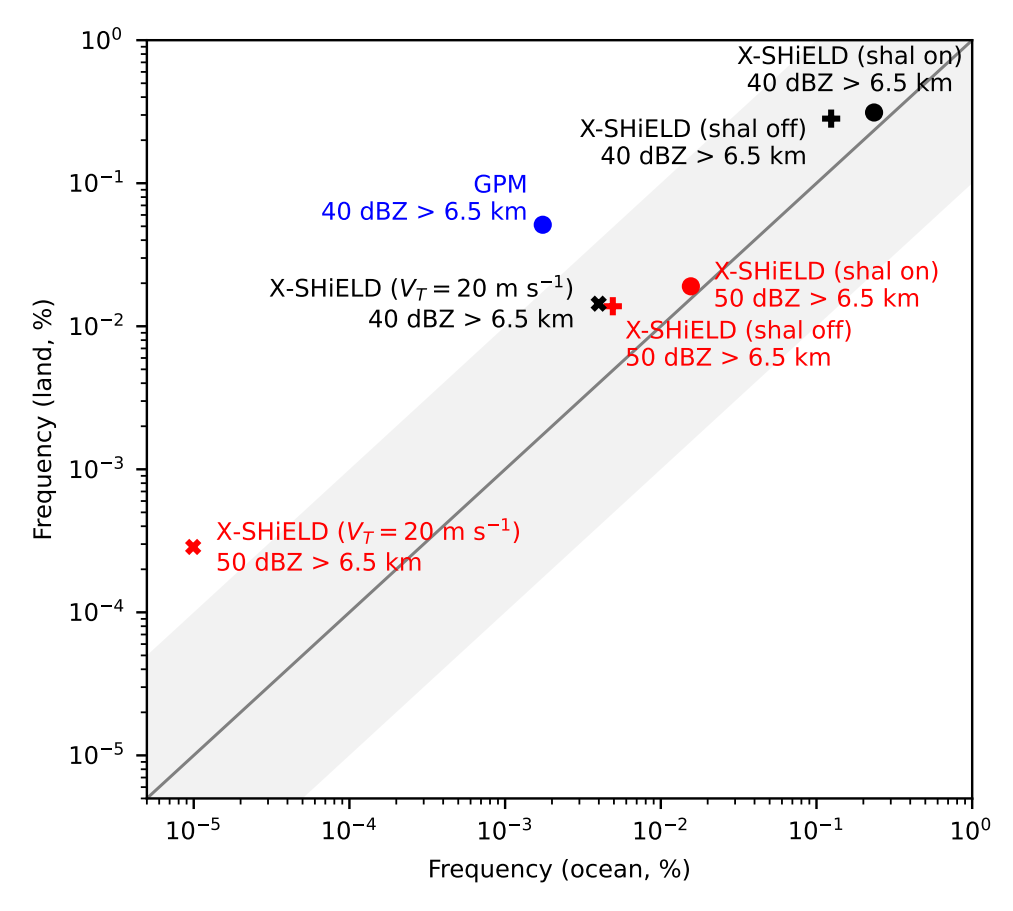


Figure S1. Land-ocean contrast indices for observed 40 dBZ echoes above 6.5 km (blue, reproduced from Figure 2 in the main text) and simulated 40 dBZ (black) and 50 dBZ (red) echos above 6.5 km in X-SHiELD simulations with parameterized shallow convection enabled (circles), parameterized shallow convection disabled (crosses), and parameterized convection disabled and hydrometeor terminal fall speeds increased to 20 m s⁻¹. The vertical and horizontal axes show representative land and ocean values, respectively, and gray shading separates points corresponding to land-ocean contrast indices above and below 10.

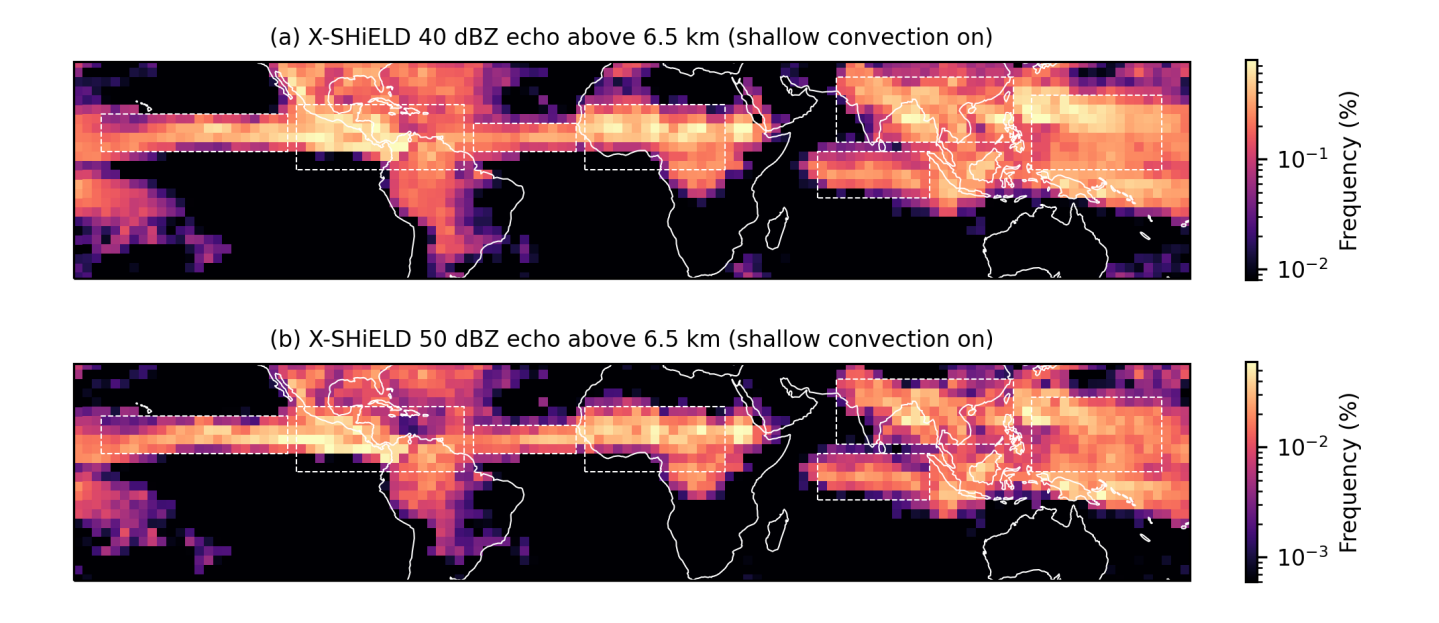


Figure S2. Frequency of 40 dBZ reflectivity above 6.5 km (a) and 50 dBZ reflectivity above 6.5 km (b) in X-SHiELD with parameterized shallow convection enabled. Dashed lines show regions used to define the land-ocean contrast indices shown in Figure S1.

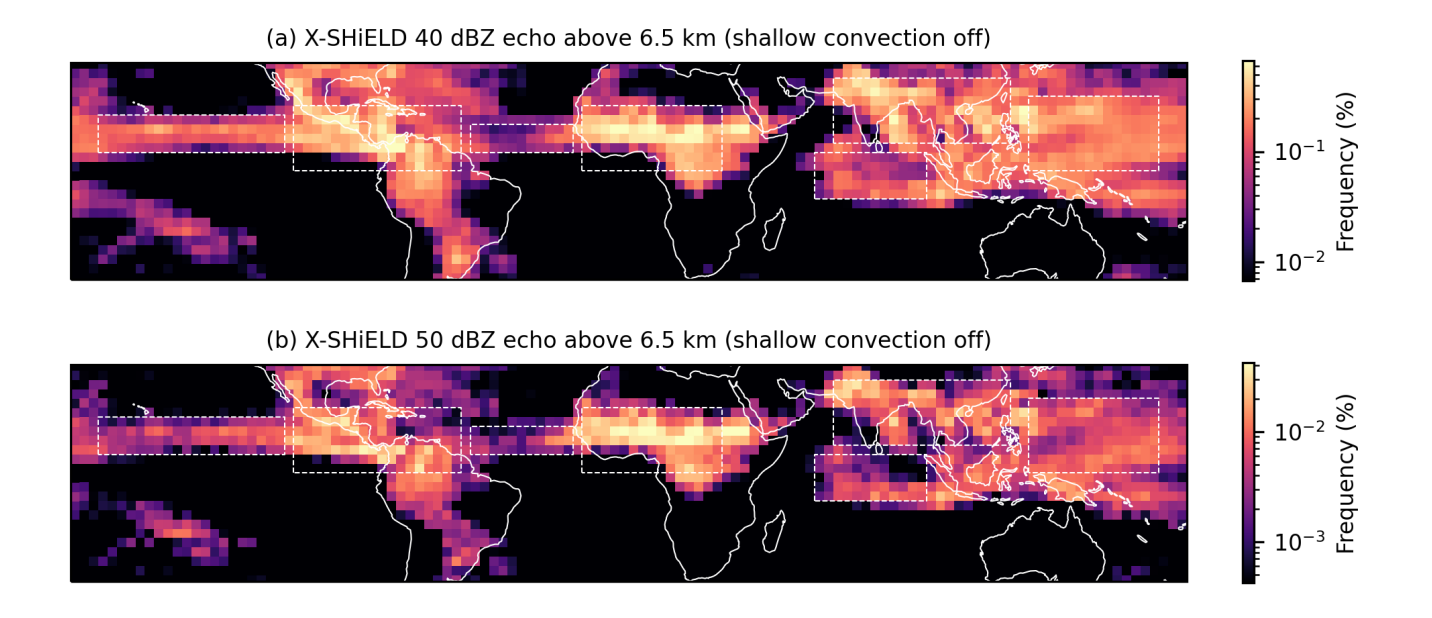


Figure S3. Frequency of 40 dBZ reflectivity above 6.5 km (a) and 50 dBZ reflectivity above 6.5 km (b) in X-SHiELD with parameterized shallow convection disabled. Dashed lines show regions used to define the land-ocean contrast indices shown in Figure S1.

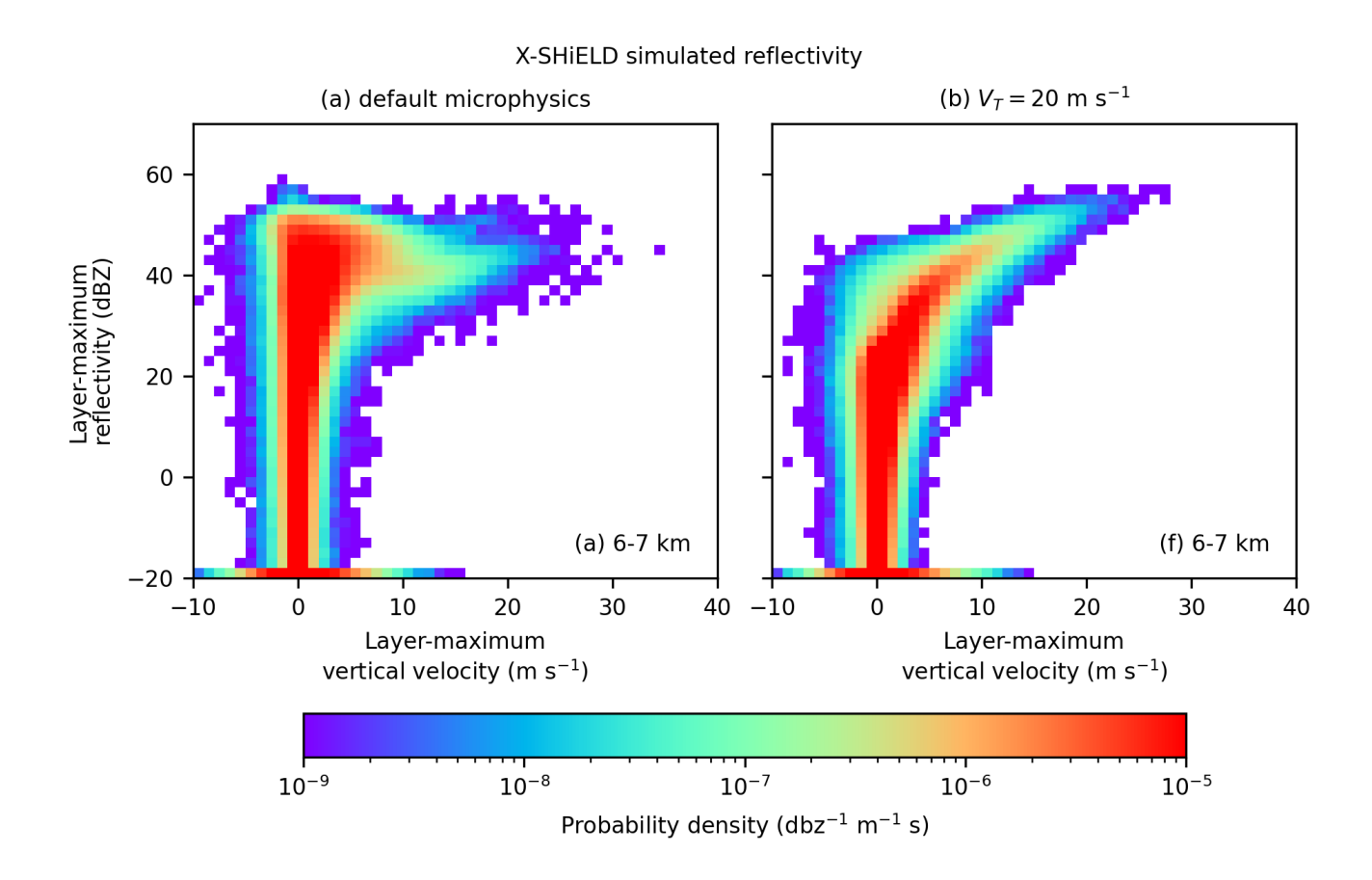


Figure S4. Joint distributions of maximum vertical velocity and reflectivity between 6 and 7 km in X-SHiELD with default microphysics (a) and with hydrometeor terminal fall speeds (V_T) set to 20 m s⁻¹ (b). Parameterized shallow convection is disabled for both simulations, and distributions are computed for days 2-10 of both simulations for consistency.

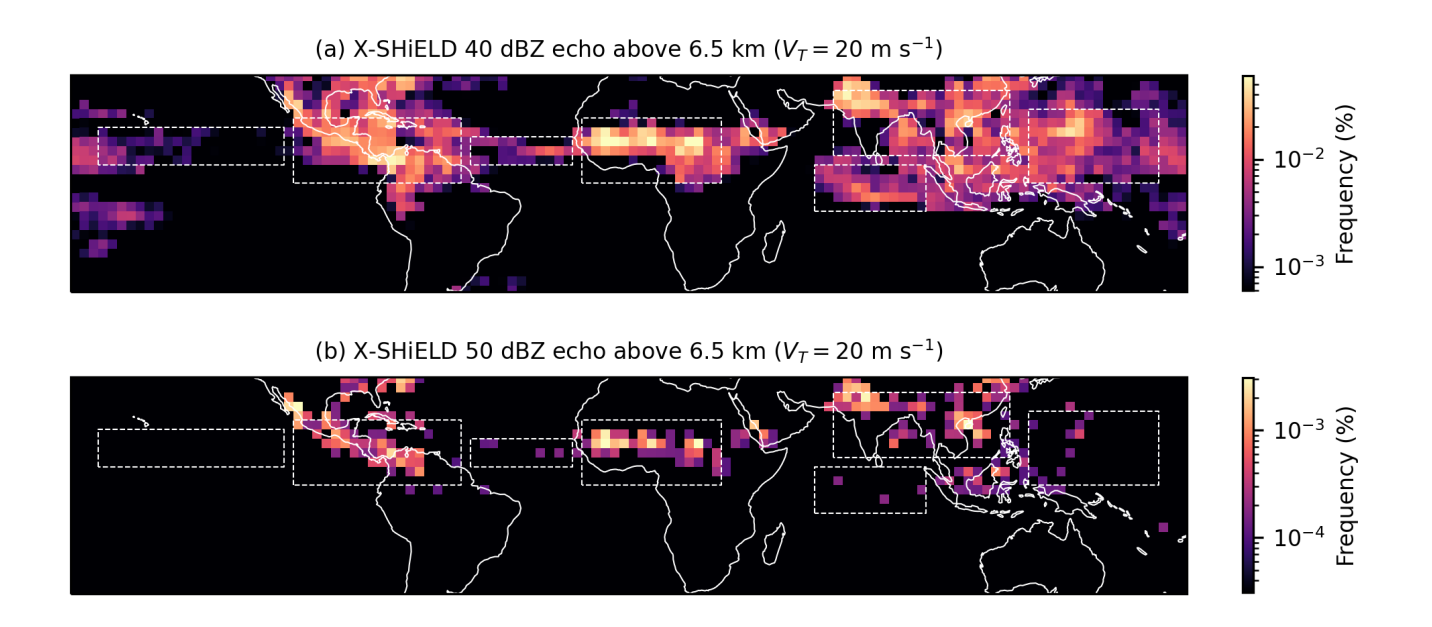


Figure S5. Frequency of 40 dBZ reflectivity above 6.5 km (a) and 50 dBZ reflectivity above 6.5 km (b) in X-SHiELD with parameterized shallow convection disabled hydrometeor terminal fall speeds (V_T) set to 20 m s⁻¹. Dashed lines show regions used to define the land-ocean contrast indices shown in Figure S1.

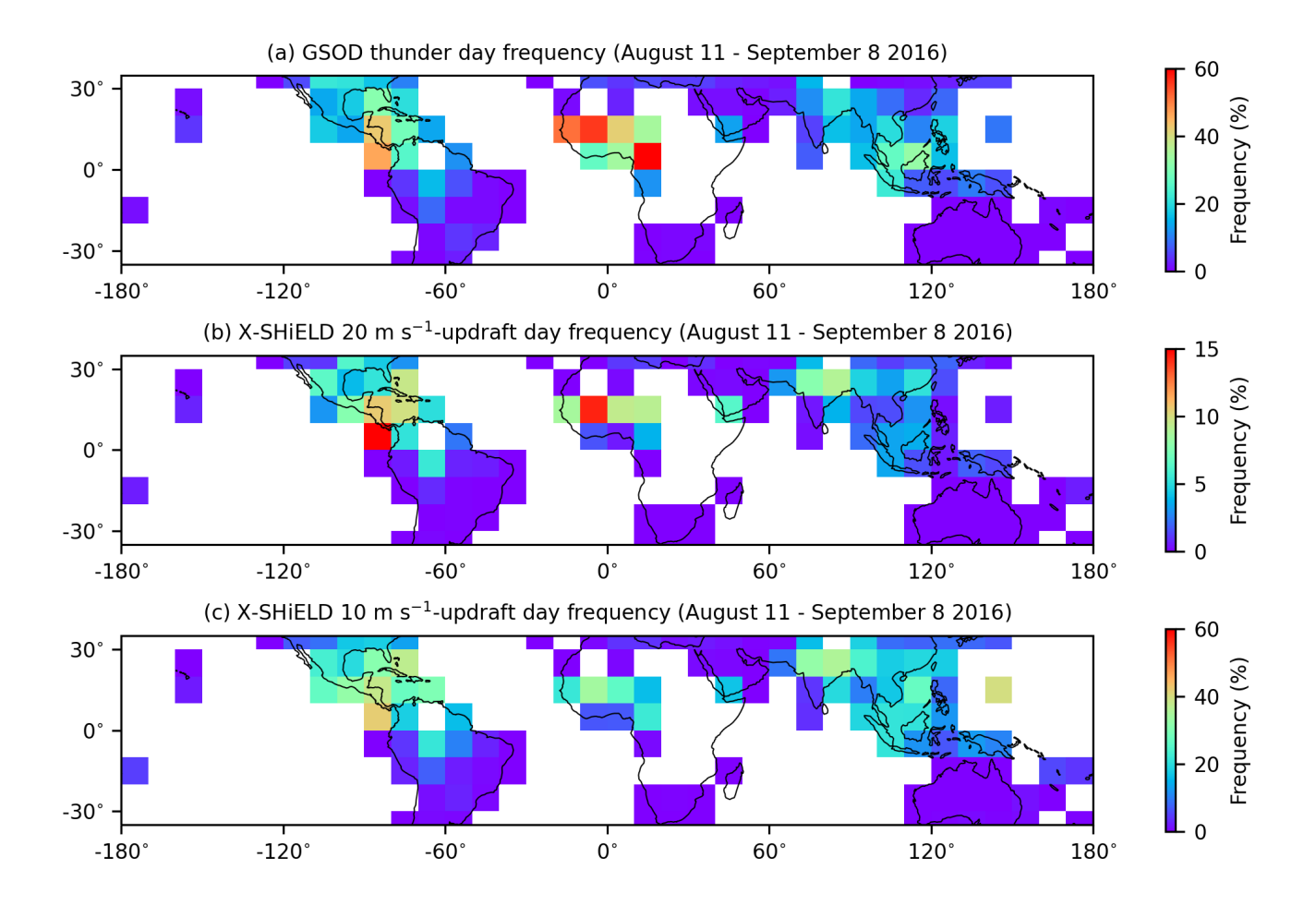


Figure S6. Observed thunder day frequencies derived from NOAA GSOD ground station observations between 11 August and 8 September 2016 (a), and simulated 20 m s⁻¹ (b) and 10 m s⁻¹ (c) "updraft-day frequencies", derived from an X-SHiELD simulation over the same period by tracking whether at least one ≥ 20 m s⁻¹ or ≥ 10 m s⁻¹ updraft occurs within 15 km of each GSOD station locations on each day. Parameterized shallow convection is disabled in the X-SHiELD simulation. Note that the colorbar range on panel (c) differs from panels (a) and (b).

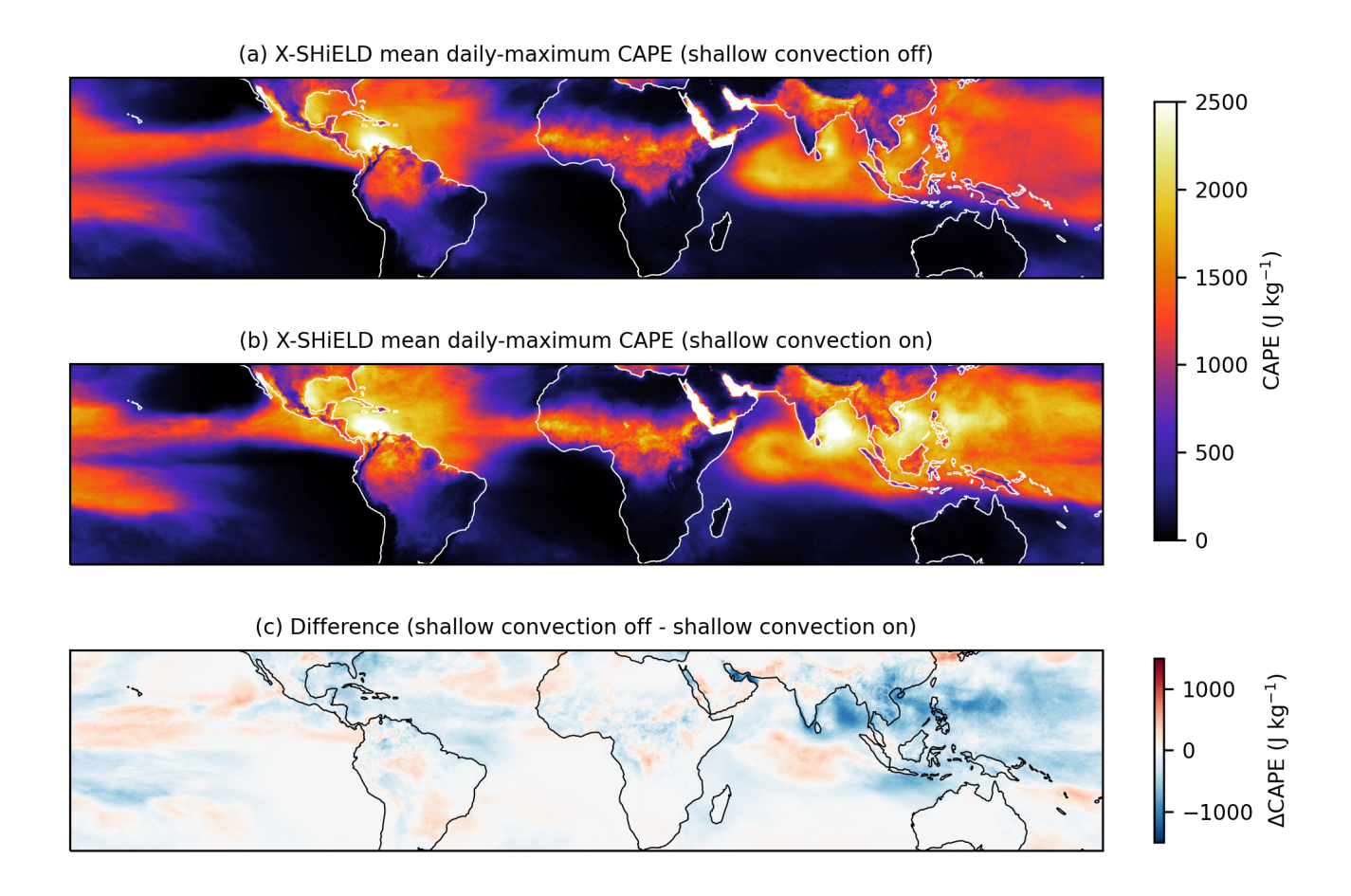


Figure S7. Average daily-maximum CAPE in X-SHiELD simulations with parameterized shallow convection disabled (a) and enabled (b), and the difference between the two simulations (c).

X - 20 :

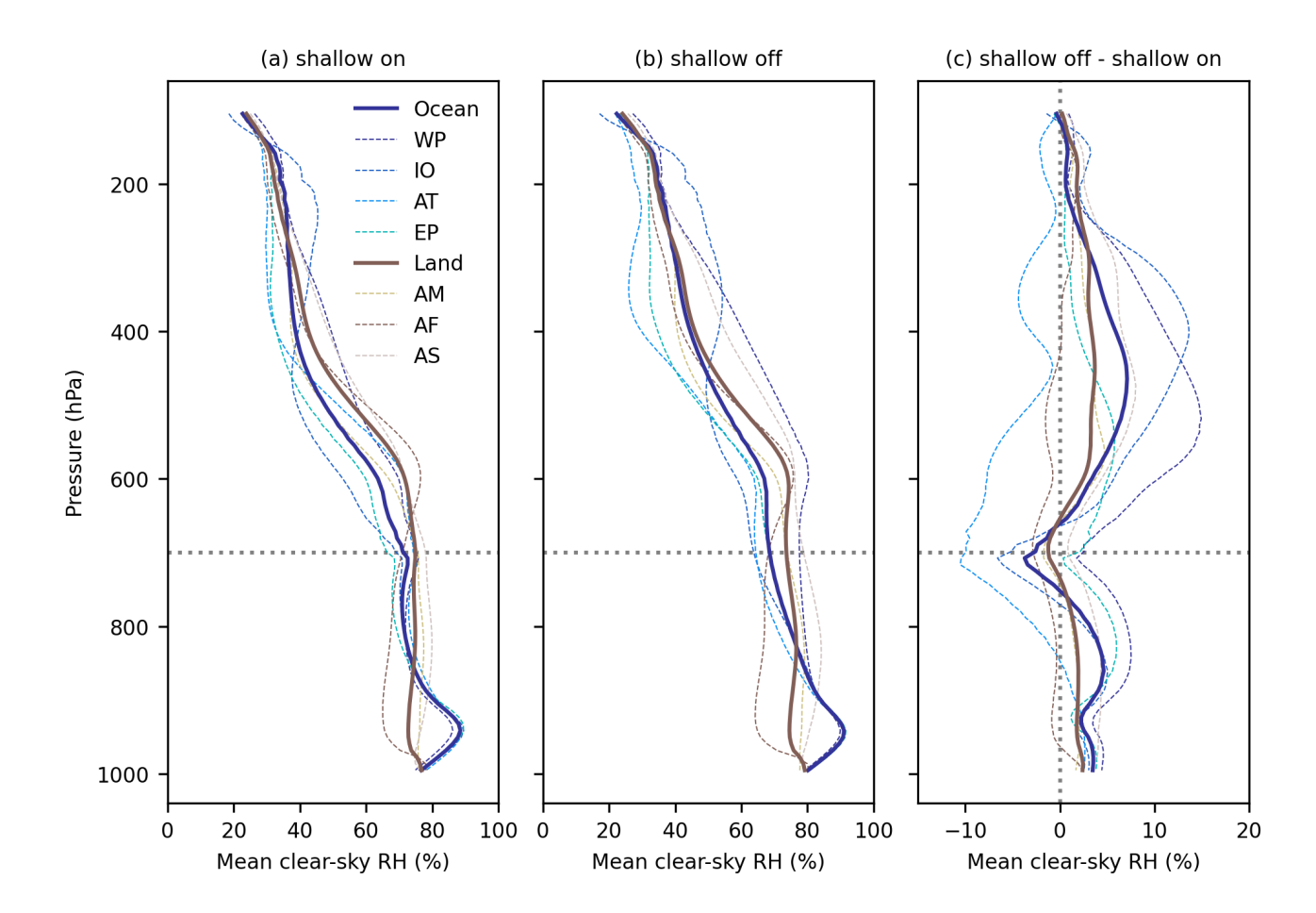


Figure S8. Mean clear-sky relative humidity profiles in X-SHiELD simulations with parameterized shallow convection enabled (a) and disabled (b), and their difference (c). Thin dashed lines show averages over each individual ocean and land region used in the calculation of land-ocean contrast indices (WP: western Pacific; IO: Indian Ocean; AT: tropical Atlantic; EP: eastern Pacific; AM: Americas; AF: western and central Africa; AS: southeast Asia). Thick solid lines show simple averages of profiles for the four ocean regions and three land regions. Clear-sky grid cells are defined as those where the total cloud water mass fraction (liquid plus ice) is below 10⁻⁵ kg kg⁻¹. The gray horizontal dotted line is at 700 hPa, where the shallow convection scheme is capped and forced to detrain any remaining mass flux.

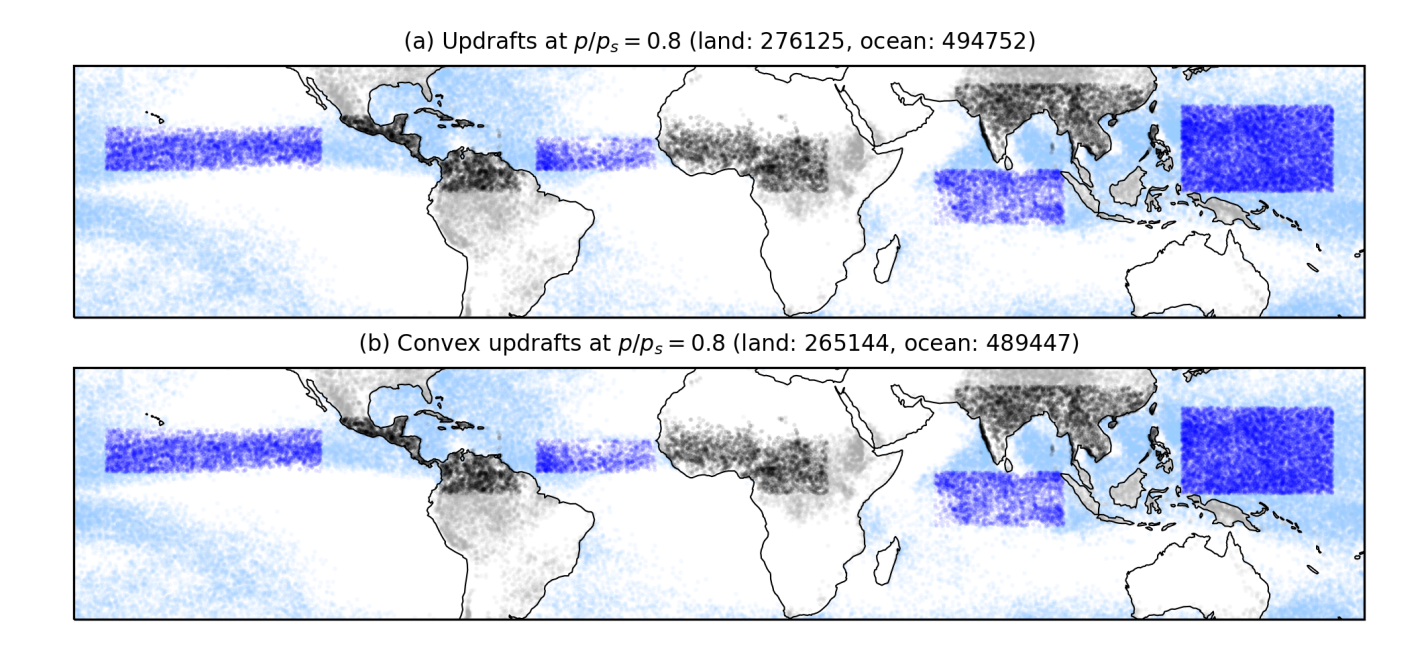


Figure S9. Locations of updrafts identified by the low-level updraft identification algorithm in the X-SHiELD simulation with parameterized shallow convection disabled. Panel (a) shows the locations of 100,000 identified updrafts, and panel (b) shows the same updrafts after filtering for a convex cross-section. Locations of updrafts are plotted using semitransparent black dots over land and semitransparent blue dots over ocean. Only updrafts inside the regions used to define the land-ocean contrast index are retained for analyses of updraft width. Pale dots indicate discarded updrafts. Counts in titles indicate the total number of retained updrafts (dark dots) over land and ocean.

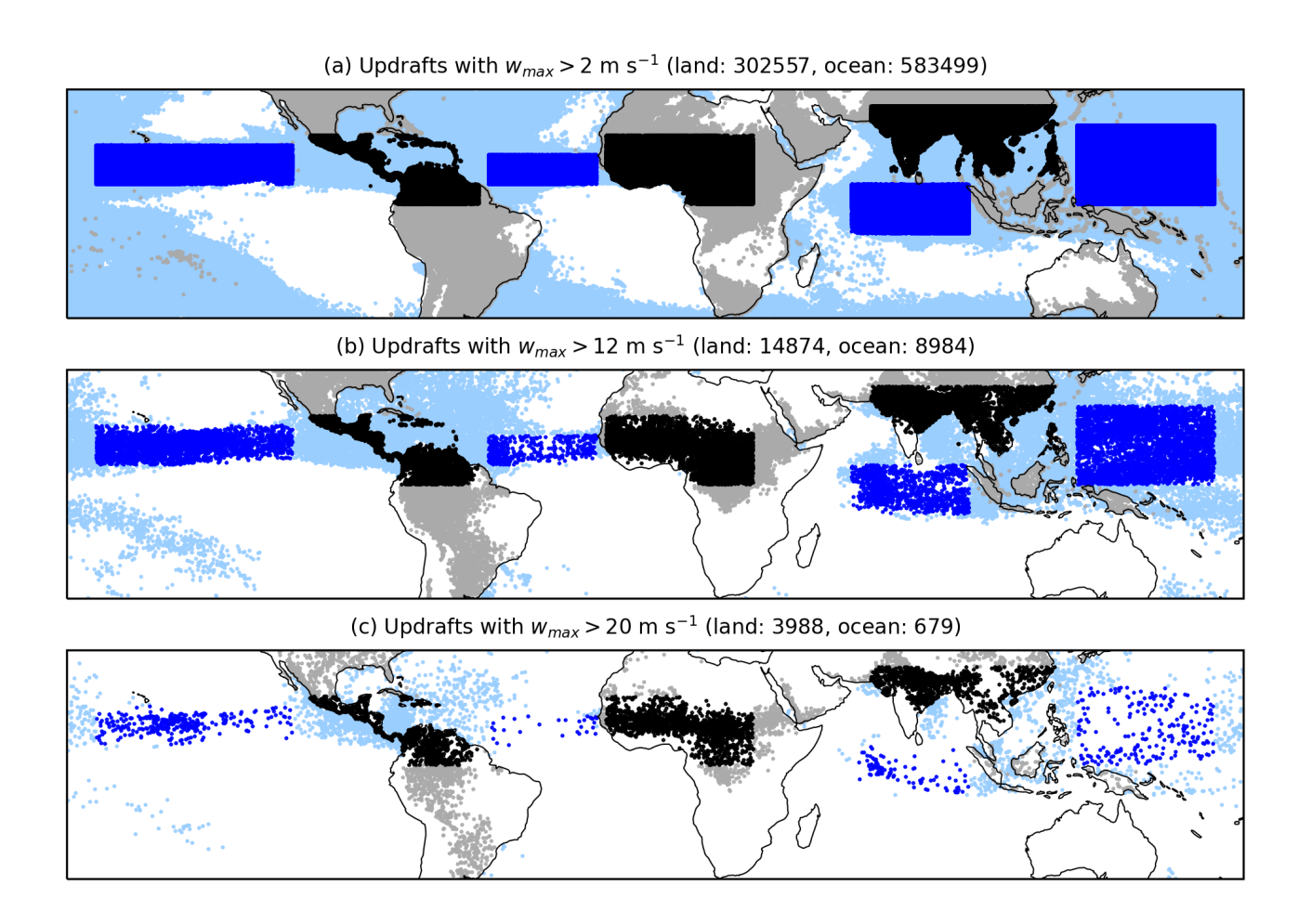


Figure S10. Locations of updrafts identified by the 3D updraft identification algorithm in the X-SHiELD simulation with parameterized shallow convection disabled. Plotted updrafts are filtered for $w_{max} > 2 \text{ m s}^{-1}$ (a), 12 m s⁻¹ (b), and 20 m s⁻¹ (c). Locations of updrafts are plotted using black dots over land and blue dots over ocean. Only updrafts inside the regions used to define the land-ocean contrast index are retained for analyses of updraft widths. Pale dots indicate discarded updrafts. Counts in titles indicate the number of retained updrafts (dark dots) over land and ocean.

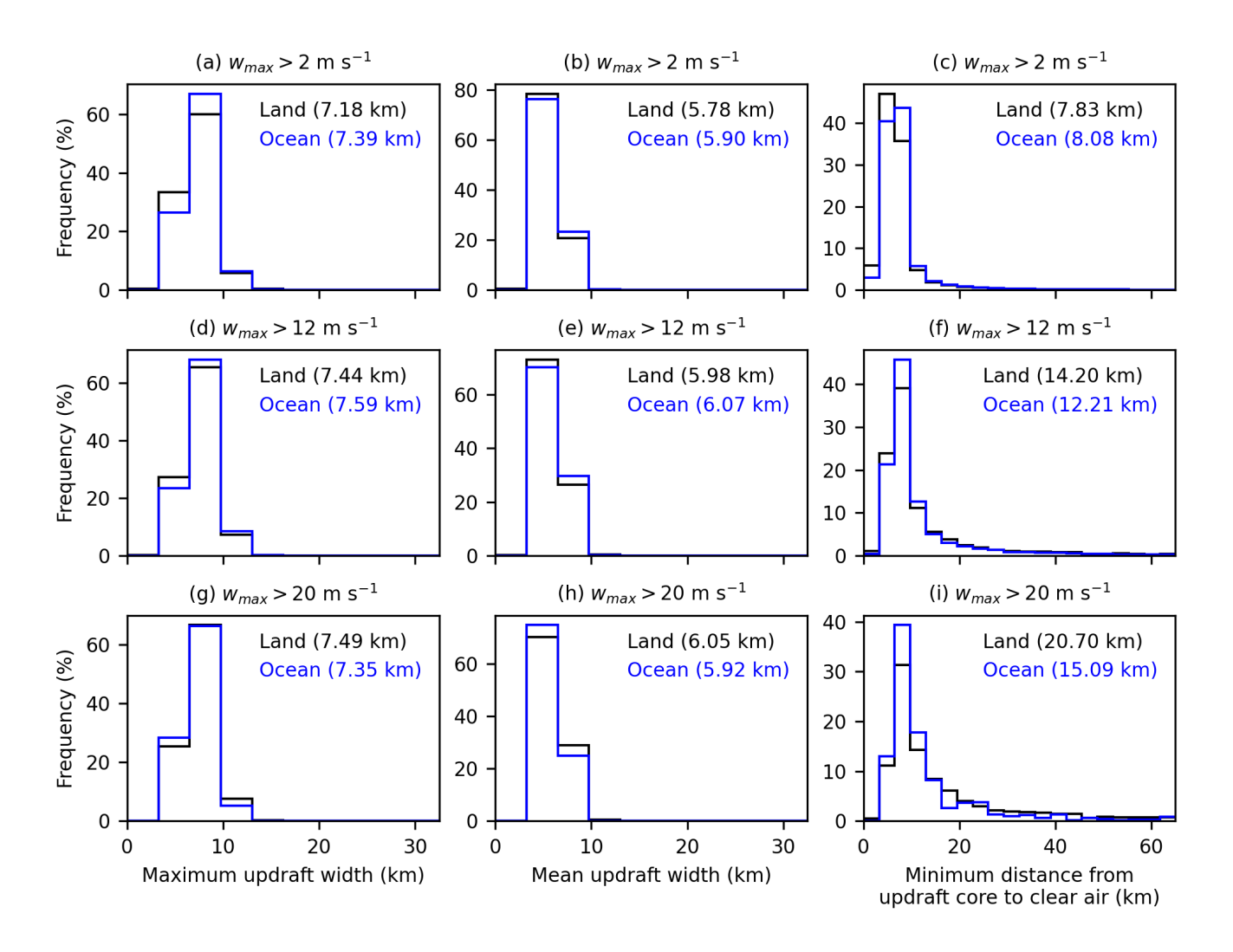


Figure S11. Histograms of maximum updraft widths (a,b,g), mean updraft widths (b,e,h), and minimum horizontal distances from updraft cores to clear air (c,f,i) in X-SHiELD with parameterized shallow convection disabled. Only updrafts within the tropical land and ocean regions defined in Section 2 of the main text are included in the histograms. Histograms for updrafts over land are shown in black, histograms for updrafts over ocean are shown in blue. Updrafts are filtered for $w_{max} > 2 \text{ m s}^{-1}$ in panels a-c; for $w_{max} > 12 \text{ m s}^{-1}$ in panels d-f; and for $w_{max} > 20 \text{ m s}^{-1}$ in panels g-i. Means for each histogram are shown in parentheses in panel legends.

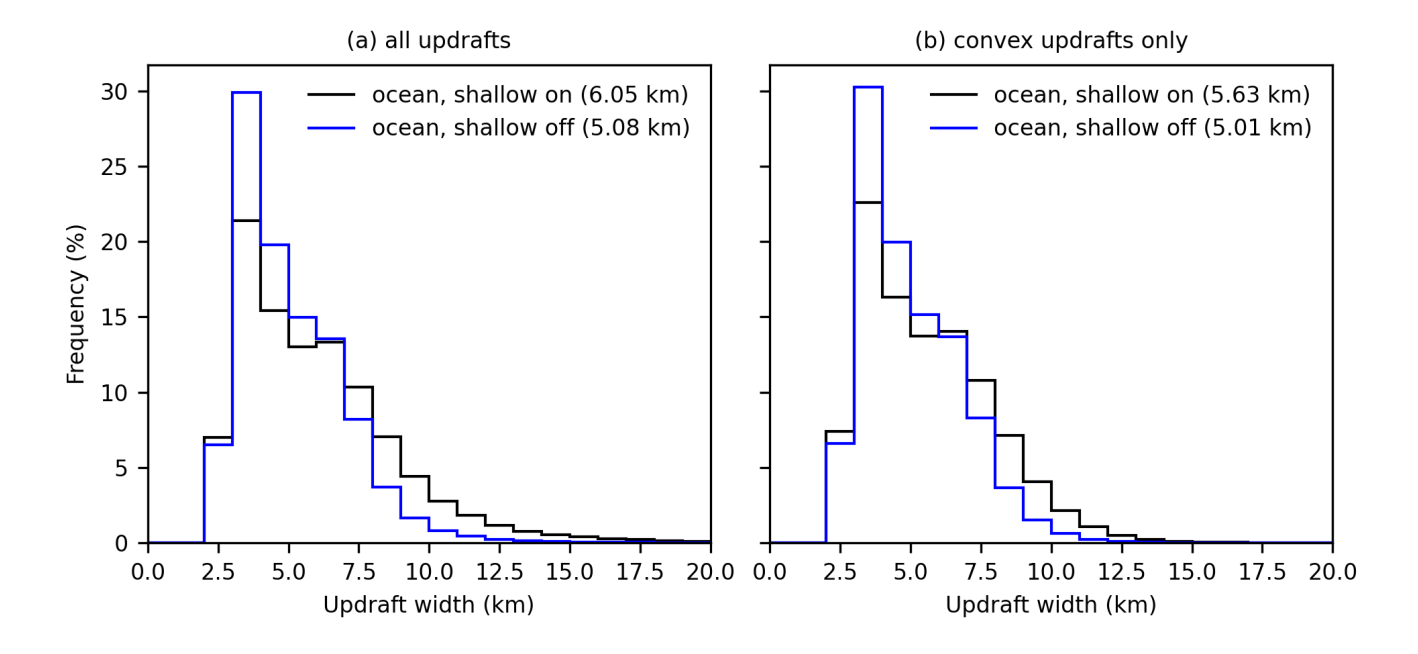


Figure S12. Distributions of low-level updraft widths over ocean in X-SHiELD with parameterized shallow convection enabled (black) and disabled (blue). Only updrafts within the tropical ocean regions defined in Section 2 of the main text are included. Distributions in panel (a) include all identified updrafts, and distributions in panel (b) include only updrafts with convex cross-sections. Means for each distribution are shown in parentheses in panel legends.